XIX International Conference on Water Resources
CMWR 2012
University of Illinois at Urbana-Champaign
June 17-22, 2012

LOCK-EXCHANGE GRAVITY CURRENTS WITH SMALL VOLUME OF RELEASE PROPAGATING OVER BOTTOM-MOUNTED OBSTACLES

Talia E. Tokyay[*] and George Constantinescu[†]

[*] University of Illinois at Urbana-Champaign
Department of Civil and Environmental Engineering
205 N. Mathews, Urbana, IL 61801 USA
e-mail: ttokyay@illinois.edu

[†] University of Iowa
Department of Civil and Environmental Engineering
300 S. Riverside Drive, Iowa City, IA 52242 USA
e-mail: sconstan@engineering.uiowa.edu

Key words: Large eddy simulation, gravity currents, lock-exchange, roughness elements

Summary. Large Eddy Simulation (LES) is used to investigate the evolution of gravity currents with a small volume of release propagating in a horizontal channel containing a series of identical large-scale obstacles. Simulations are conducted at a Reynolds number defined with the buoyancy velocity and the channel half depth ($Re=u_b(H/2)/\nu$) of 47,800. 2-D dunes and ribs are considered as roughness elements. Results show that the gravity current propagating over an array of obstacles transitions from buoyancy-inertia regime where average front velocity decays proportionally with $t^{-1/3}$ to a regime where turbulent-drag is dominated. In turbulent-drag dominated regime, the average front velocity decays faster proportional to $t^{-1/2}$.

1 INTRODUCTION

In this study, the case of lock-exchange compositional currents is considered (see Fig. 1). All the simulations focus on partial-depth release (h=H/2) lock exchange currents in which the top interface of the gravity current is situated well beneath the free surface. The initial volume of release is relatively small ($x_0/(H/2)=0.56$, H is the channel depth) such that the backward propagating current starts interacting with the rear end-wall a short time after the removal of the lock gate. As the lighter current starts interacting with the rear wall, it reflects and forms a bore or a hydraulic jump that propagates in the same direction as the heavier current. The bore speed, U_{bore}, is nearly constant and slightly higher than the front velocity (U_f). Meanwhile, the head of the heavier current propagates with practically constant depth and constant velocity (U_f). For sufficiently high Reynolds numbers, once the bore catches the front, the heavier current transitions to the buoyancy-inertia self-similar phase in which the motion of the current is determined by a balance between the inertial and gravitational (buoyancy) forces, and the front velocity decays with time following a power law ($U_f \sim t^{-1/3}$). If the channel is long enough such

that viscous effects become dominant, the current will transition to the viscous-buoyancy self-similar phase in which the motion of the current is determined by a balance between the viscous and gravitational forces. The flow at the front decelerates faster as $U_f \sim t^{-4/5}$ (see [1, 2]). The buoyancy-inertia phase may not be present if the Reynolds number is sufficiently low [2, 3].

In the case in which the bed surface is rough or a porous layer (e.g., vegetation layer) is present close to the bed, the volume of release is sufficiently large, and the drag force acting on the gravity current as a result of the presence of a rough bed is significant, a buoyancy-turbulent drag flow regime can be present in between the buoyancy-inertia and the viscous-buoyancy self-similar phases [4]. As the initial volume of release increases, the time interval over which the drag-controlled regime is present increases. Over this regime the front speed decreases with time as $U_f \sim t^{-1/2}$. The faster decrease of the front velocity compared to the one expected over the buoyancy-inertia phase is due to the added action of the drag induced by the presence of a deformed surface, a rough bed or a porous layer.

2 NUMERICAL METHOD

The numerical solver is a finite-volume DNS / LES code. A detailed description of the code and computational technique is available in [5, 6]. The algorithm discretely conserves energy, which allows obtaining solutions at high Reynolds numbers in the LES regime without artificial damping. All operators are discretized using central discretizations, except the convective term in the advection-diffusion equation solved for the concentration for which the QUICK scheme is used. The code is parallelized using MPI.

In the present study the density differences between the lock fluid and the ambient fluid are kept small enough such that the Boussinesq approximation is valid. The filtered continuity and momentum equations and the advection-diffusion equation for the concentration $\overline{C}$ are made dimensionless using a characteristic length scale, L, and the buoyancy velocity, $u_b = \sqrt{g' L}$, ($g' = g(\overline{C}_{\max} - \overline{C}_{\min})/\overline{C}_{\max}$, $\overline{C}_{\max}$ and $\overline{C}_{\min}$ are the maximum and minimum initial concentrations in the domain, g is the gravitational acceleration).

$$\frac{\partial u_i}{\partial t} + \frac{\partial (u_i u_k)}{\partial x_k} = -\frac{\partial p}{\partial x_i} + \frac{\partial}{\partial x_k}\left[\left(\frac{1}{\sqrt{Gr}} + \nu_{SGS}\right)\left(\frac{\partial u_i}{\partial x_k} + \frac{\partial u_k}{\partial x_i}\right)\right] - C\delta_{i2} \tag{1}$$

$$\frac{\partial C}{\partial t} + \frac{\partial (C u_k)}{\partial x_k} = \frac{\partial}{\partial x_k}\left(\left(\frac{1}{\sqrt{Gr}Sc} + \alpha_{SGS}\right)\frac{\partial C}{\partial x_k}\right) \tag{2}$$

In Eqn. 1, p and u_i are the dimensionless pressure and Cartesian velocity component in the i direction. The dimensionless concentration is defined as $C = (\overline{C} - \overline{C}_{\min})/(\overline{C}_{\max} - \overline{C}_{\min})$ and is linearly related to the density ρ.

3 SIMULATION DOMAIN AND BOUNDARY CONDITIONS

In the analyses of the simulation results, the channel half depth, H/2, is used for scaling the lengths. The buoyancy velocity $u_b = \sqrt{g'(H/2)}$ is used for scaling the velocities. The time scale of the simulations is $t_0=(H/2)/u_b$. The 2-D dunes have a ratio between their height, D, and their wavelength, λ, of 0.05 (see Fig. 1). The shape of the dunes is taken from an experimental study[7]. The effect of the shape of the obstacles is studied based on the differences observed in simulations conducted with dunes and ribs of equal height (D=0.15(H/2)) and equal wavelength (λ=3(H/2), λ/D=20). The center of each rib is situated at the location of the crest of the corresponding dune. In all the simulations the center/crest of the first obstacle was situated at x/(H/2)=5. The ratio λ/D=20 corresponds to the k-type roughness regime, which is the relevant one for most practical applications in geosciences.

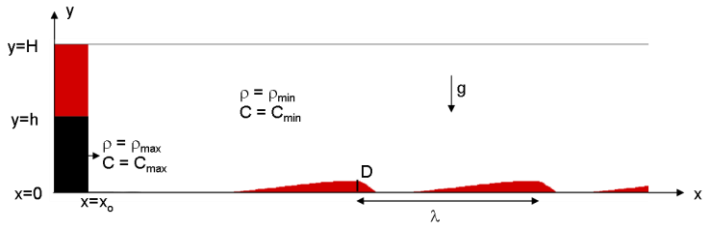

Figure 1: Sketch of a partial-depth lock-exchange flow with a low volume of release ($R=x_0/h=O(1)$) before the lock gate was removed. The bottom is a no-slip surface. The dunes are positioned on the bottom surface to the right of the lock gate.

In all the simulations, the grid size was 3000×64×188 in the streamwise (domain length $L_1=21.5(H/2)$), spanwise (domain width $L_3=(H/2)$), and vertical (domain height $L_2=H$) directions, respectively. The simulations are conducted with no-slip boundary conditions at the bottom surface. The top surface of the channel was treated as a non-deformable slip boundary. A zero normal gradient was imposed for the concentration at the top, bottom and end-wall boundaries. The non-dimensional concentration field was initialized with a constant value of one in the region containing the lock fluid and a constant value of zero in the rest of the computational domain. The time step was $0.001t_0$. For most simulations, the total simulation time was around $70t_0$.

4 RESULTS

Fig. 2 shows the distributions of the non-dimensional concentration C, streamwise velocity u/u_b and out-of-plane vorticity $\omega_z(H/2)/u_b$ for the simulation with a flat bed (SV-LR-F) when $x_f/(H/2)\sim18$, well after the end of the slumping phase. As observed in Fig. 2c a strong shear layer forms at the interface between the head and the ambient fluid. The vorticity remains high over the head and dissipative wake, not only over the interfacial region but also within the body of the current. The height of the region of high concentration fluid decays sharply over the dissipative wake region. The billows shed behind the head mix the high concentration fluid ejected from the

head with the surrounding ambient fluid. This results into the presence of a region of mixed fluid, of concentration slightly higher than zero, for some distance behind the head. Over the downstream part of the tail region (10<x/(H/2)<15), the velocity decrease with the distance from the front is close to monotonic (see Fig. 2b). The velocity is close to zero over the tail region where x/(H/2)<10. As we move away from the dissipative wake region, the coherence of the billows reduces gradually and a layer of mixed fluid develops (Fig. 2a). As also shown by the vorticity distribution in Fig. 2c, the decay in the coherence of the interfacial billows is accompanied by an overall decay of the strength of the turbulent eddies within the body of the current and the interfacial region. Over the tail region for x/(H/2)<10, flow tries to relaminarize.

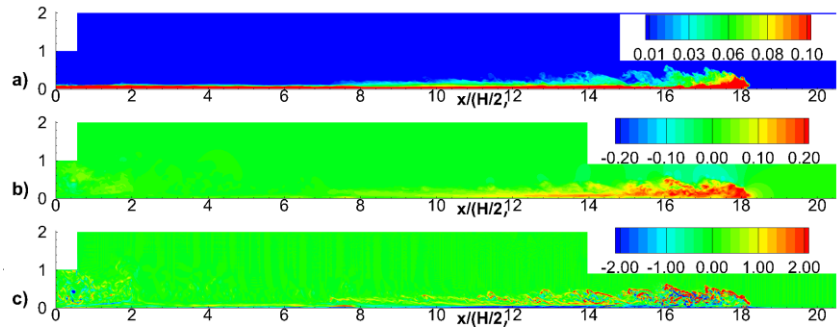

Figure 2: Structure of the gravity current at a time when the front is situated close to $x_f/(H/2)=18$ in the SV-LR-F simulation. a) concentration, C; b) streamwise velocity, u/u_b ; c) out-of-plane vorticity, $\omega_z(H/2)/u_b$. The aspect ratio is 1:2 in the x-y contour plots.

The presence of large-scale roughness elements at the bed induces important quantitative changes in the structure of the gravity current compared to the flat bed case. However, at a qualitative level, the structure of the gravity current, at large times after the lock-fluid was released, is not very different. Most of the kinetic energy is concentrated in the head and dissipative wake regions.

In the case of dunes, the flow goes supercritical (maximum Froude number is Fr=1.5-2) in the jet-like flow forming over the lee side of the first and second dunes, when the current overtakes the second obstacle in the series as shown in Fig. 3a. The fact that Fr>1 over the crest of Dune1 are due to the very small depth of the layer of higher density fluid over the crest of the first dune. Fig. 3b shows that in later stages of the simulation similar phenomenon is observed for higher rank of dunes. As the flow passes the fifth dune in the domain the Froude number increases at the crest of both Dune4 and Dune5. Another increase in the Froude number is observed around the crest and upslope of Dune3 due to the passage of a backward propagating disturbance. The passage of the disturbance propagating upstream, which carries small amount of heavier fluid, causes an increase in the depth and the velocity of the current over that region. Though the flow is clearly supercritical downstream of the crest of Dune5 in Fig. 3b, the maximum value of the Froude number is smaller than that recorded as the front passed Dune2 in Fig. 3a. Over the head

of the current Froude number is close to unity at all stages of the flow.

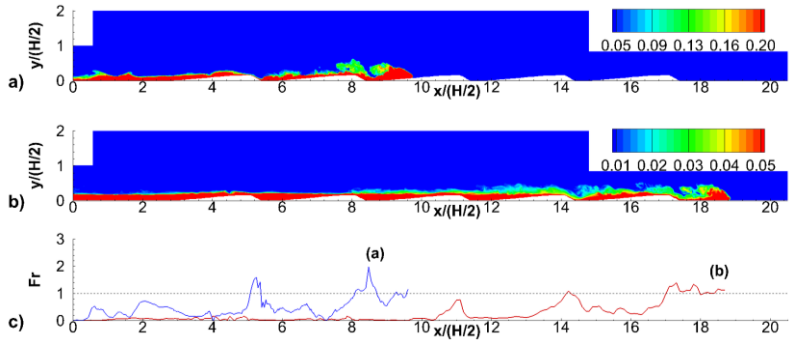

Figure 3: Streamwise distribution of the Froude number in the SV-LR-D15 simulation. The structure of the current is visualized in an x-y section using concentration contours. a) $x_f/(H/2)=9.5$ (buoyancy-inertia phase); b) $x_f/(H/2)=18.5$ (drag-dominated phase); c) variation of Froude number along the body of the current for both phases.

The structure of the current in the SV-LR-R15 simulation is, in many regards, similar. The Froude numbers in the head region are very close to unity during the buoyancy inertia and the drag dominated phases. Also, the flow past the second rib behind the front is supercritical or gets close to critical over a very short distance. Similar to the simulation with dunes, this is mostly due to a flow disturbances propagating downstream.

In the simulations with a flat bed, the main reason the front velocity starts decaying are the frictional losses at the channel bottom and the losses from mixing at the current interface. As expected, the presence of ribs or dunes slows down the advancement of the front of the current compared to the flat-bed case due to the additional drag induced by the roughness elements. In the simulations with obstacles of same height, as the ribs have a higher degree of bluntness than dunes, the form drag component is higher. Consequently, the distance traveled by the front at a certain non-dimensional time in the simulation with ribs is smaller. Fig. 4 shows the front position of the current in time in log-log scale. The current propagating over flat bed transitions to buoyancy-inertia phase after a short slumping phase and stays in this phase until the end of simulation. In the slumping phase the front velocity of the current is proportional to t^{-1}, while in the buoyancy-inertia phase the front velocity of the current is proportional to $t^{-1/3}$ as given by the dotted and dashed slope lines, respectively. In the presence of the roughness elements transition from slumping to buoyancy-inertia phase happens faster however current does not stay in this phase but further slows down and gets dominated by the drag force due to the obstacles. In the drag dominated regime the front velocity of the current becomes proportional to $t^{-1/2}$ as indicated in the figure with dash-dotted lines.

The time evolutions of the kinetic energy E_k, potential energy E_p and integral of the total dissipation rate, E_d are plotted in top row of Fig. 5. The three terms are nondimensionalized by E_{p0}, initial potential energy of the flow. The current starts interacting with the first obstacle

around $t=5t_0$, during the slumping phase, when $x_f/(H/2)\sim3$. As expected, in the simulations with obstacles, once the current starts interacting with the first obstacle, the decay of the kinetic energy is faster compared to the flat bed case because of the additional obstacle-induced drag force acting on the body of the current. Conversely, the decay of E_p with time is slower. The variation of E_d with time is close to identical in the SV-LR-F and SV-LR-R15 simulations. This can be surprising at first, as we expect a gravity current propagating over obstacles to be more dissipative. However, the current in the SV-LR-F simulation propagates faster. Thus, its length is larger at a given non-dimensional time. To make the comparison more meaningful, the variations of E_d is plotted as function of the front position, $x_f/(H/2)$, in Fig. 5d. When plotted with the front position, E_d increases faster in the simulation with ribs. The variations of E_k and E_p with time in the SV-LR-R15 and SV-LR-D15 simulations are subject to large-scale modulations induced by the interaction of the current with the obstacles. As the front approaches the obstacle, the head starts decelerating and the kinetic energy starts decreasing in that region. As the splash forms, the downstream part of the current containing heavier fluid raises and the potential energy in the front region increases. The kinetic energy increases again after the splash was convected over the obstacle and the head regains its usual shape.

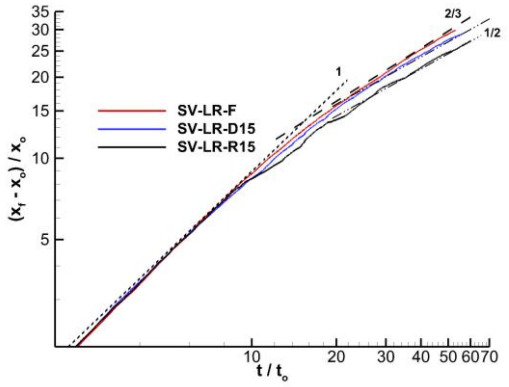

Figure 4: Time variation of the non-dimensional position of the front, $(x_f-x_0)/x_0$, function of the non-dimensional time, t/t_0 (log-log scale) in the simulations SV-LR-F, SV-LR-D15 and SV-LR-R15.

Comparison of Figures 6a and 6c shows that the distribution of u_τ over the head and dissipative wake is qualitatively and quantitatively similar in the simulations with a flat bed and with ribs, at time instants when the front is situated at more than (H/2) from the last rib it passed but has not start interacting with the next rib. In the SV-LR-D15 simulation, the streamwise variation of u_τ is much more complex. The values of u_τ peak immediately in the trough region, where the flow is strongly accelerated and transitions to supercritical as well as at the head of the current as shown in Fig. 6b at around $x/(H/2) \sim 5.1$. The u_τ values decrease over the upslope of the next dune because the incoming heavier fluid has a significant amount of streamwise momentum and tries to separate. The distribution of u_τ behind the dissipative wake, and in particular the position of the spanwise bands of high u_τ values, is quite different in the three simulations. This is because the positions and the strengths of the disturbances propagating on

the interface of the gravity current are different. For example, the band of high u_τ values (indicated with dashed lines in Fig. 6c) centered around x/(H/2)=3 in the SV-LR-R15 simulation is due to the passage of the backward propagating disturbance. These disturbances exist even at later stages of the simulation affecting the shear velocity distribution near the bed.

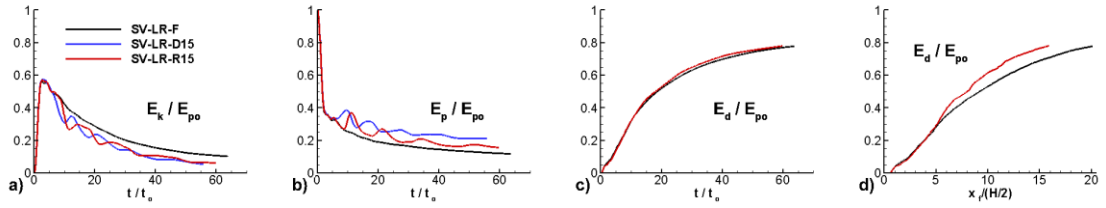

Figure 5: Variation of the potential energy, E_p, kinetic energy, E_k, and integral of the total dissipation, E_d, with respect to time (a, b, c) and variation of E_d with front position (d) in the SV-LR-F, SV-LR-D15 and SV-LR-R15 simulations.

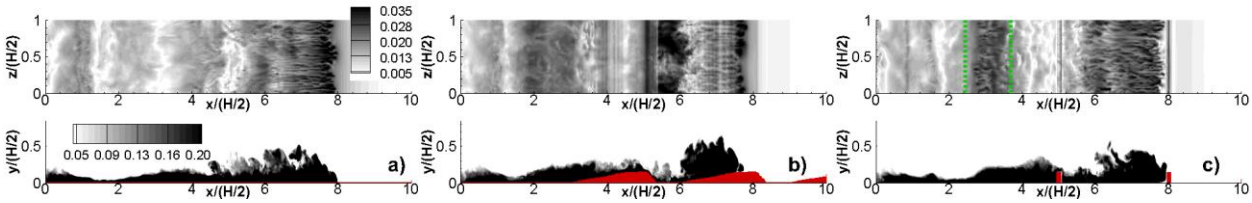

Figure 6: Spatial distribution of the bed friction velocity, u_τ/u_b, during the buoyancy-inertia phase when the front position is $x_f/(H/2)=8$. a) SV-LR-F simulation; b) SV-LR-D15 simulation; c) SV-LR-R15 simulation. Also shown are the concentration contours in an x-y section. The aspect ratio is 1:2 in the x-y plots.

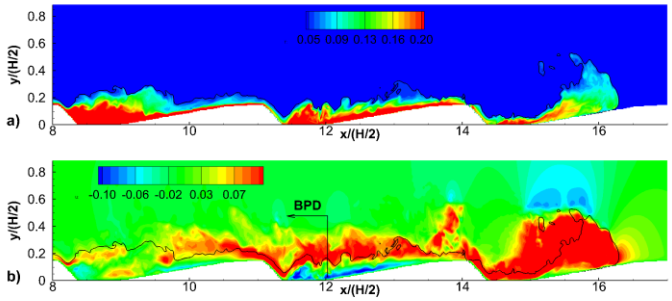

Figure 7: Visualization of the structure of the gravity current in an x-y plane between x/(H/2)=8 and the front, in the SV-LR-D15 simulation, when the front position is $x_f/(H/2)=16.5$. a) concentration; b) streamwise velocity. The solid lines correspond to the concentration isosurface C=0.05.

An example of such strong flow disturbance propagating in between the crests of the dunes is shown in Fig. 7 during drag dominated phase. Figure visualizes the distribution of the concentration and streamwise velocity in between the front and the crest of the second dune, when $x_f/(H/2)=16.2$. The interface with the ambient fluid is superimposed on the contours of the

streamwise velocity as a solid line. The streamwise velocity is negative in between the crest of Dune4 and the downstream end of the lee side of Dune3 (x/(H/2)=11.4). This coincides with the position of the disturbance BPD that originated due to reflection of some of the heavier fluid reaching the crest of Dune4.

The main difference between the distributions of u_τ during the drag-dominated regime in the SV-LR-D15 and SV-LR-R15 (the comparison is done for the same position of the front) is the significantly smaller amplification of u_τ at the downstream of the crest of the first roughness element behind the front (See Fig. 8). This is due to the larger drag force per unit length induced by the ribs. The front of the current slows down significantly in the presence of rib compared to the one propagating over dunes. The overall values of u_τ in the simulations with dunes and ribs of same height become much more comparable over the upstream part of the current. The local Reynolds number of the current is so low that there are no high and low velocity streaks formed which indicates that the tail region of the current has almost no turbulence.

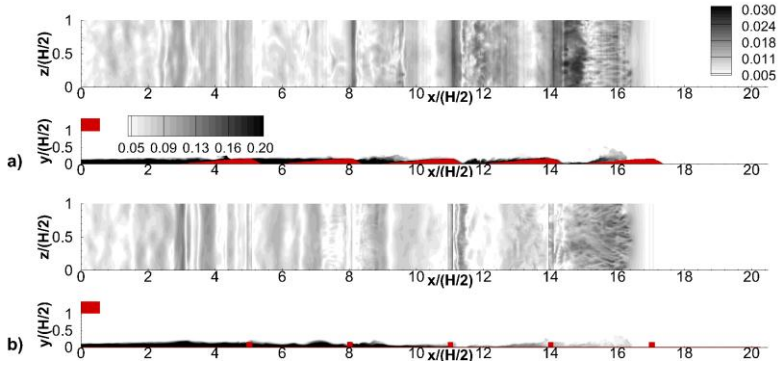

Figure 8: Spatial distribution of the bed friction velocity, u_τ/u_b, during the drag-dominated phase when the front position is $x_f/(H/2)=16.5$. a) SV-LR-D15 simulation; b) SV-LR-R15 simulation. Also shown are the concentration contours in an x-y section. The aspect ratio is 1:2 in the x-y plots.

5 CONCLUSIONS

The present investigation showed that gravity currents with a small volume of release propagating over large-scale roughness elements reach a regime in which the front velocity decays proportional to $t^{-1/2}$, similar to the case of gravity currents propagating into a porous medium. In the case of current propagating into a porous medium, the drag acts over the whole height of the current rather than only over the bottom layer of the gravity current. The variations of E_k and E_p with time were subject to large-scale modulations induced by the interaction of the current with the obstacles. The simulations demonstrated the important role played by the backward propagating disturbances forming at the crest/top of the roughness elements and by their reflections in transferring momentum between the upstream and the downstream part of the current. The passage of the forward and backward propagating flow disturbances was found to control the distribution of the bed shear stress magnitude and its sign over the tail of the currents.

REFERENCES

[1] Huppert, H.E., (1982), "The propagation of two-dimensional and axisymmetric viscous gravity currents over a rigid horizontal surface", Journal of Fluid Mechanics, Vol. 121, 43-58.

[2] Rottman, J.W. and Simpson, J.E., (1983), "Gravity currents produced by instantaneous releases of a heavy fluid in a rectangular channel", Journal Fluid Mechanics, Vol. 135, 95–110.

[3] Cantero, M.I., Lee, J.R., Balachandar, S., and Garcia, M.H., (2007), "On the front velocity of gravity currents", Journal of Fluid Mechanics, Vol. 586, 1-39.

[4] Hatcher, L., Hogg, A.J., Woods, A.W., (2000), "The effects of drag on turbulent gravity currents", Journal of Fluid Mechanics, Vol. 416, 297-314.

[5] Pierce, C.D., (2001), "Progress-variable approach for large eddy simulation of turbulent combustion", PhD thesis, Stanford University.

[6] Pierce, C.D. and Moin, P., (2004), "Progress-variable approach for large-eddy simulation of nonpremixed turbulent combustion", Journal of Fluid Mechanics, Vol. 504, 73–97.

[7] Mierlo, M.C. and de Ruiter, J.C., (1988). "Turbulence measurements over artificial dunes", Report Q789. Delft Hydraulics Laboratory, Delft, Netherlands.